



# IJRASET

International Journal For Research in  
Applied Science and Engineering Technology



---

# INTERNATIONAL JOURNAL FOR RESEARCH

IN APPLIED SCIENCE & ENGINEERING TECHNOLOGY

---

**Volume:** 14    **Issue:** III    **Month of publication:** March 2026

**DOI:** <https://doi.org/10.22214/ijraset.2026.78834>

[www.ijraset.com](http://www.ijraset.com)

Call:  08813907089

E-mail ID: [ijraset@gmail.com](mailto:ijraset@gmail.com)

# Synthesis and Characterization of $\text{Ba}_{0.5}\text{Sr}_{0.5}(\text{Co}_{0.8}\text{Fe}_{0.2})_{1-x}\text{Zr}_x\text{O}_{3-\delta}$ (BSCFZ) Cathode for Solid Oxide Fuel Cell

Mr.D.Rama Krishna Sharma<sup>1</sup>, Dr.P.Vijay Bhaskar Rao<sup>2</sup>

<sup>1</sup>Department of Physics, Jawaharlal Nehru Technological University, Hyderabad

<sup>2</sup>Professor and Director, R&D, St. Mary Engineering College, Deshmukhi, Hyderabad, India

**Abstract:** The BSCFZ, Barium Strontium Cobalt Iron Zirconate  $\{\text{Ba}_{0.5}\text{Sr}_{0.5}(\text{Co}_{0.8}\text{Fe}_{0.2})_{1-x}\text{Zr}_x\text{O}_{3-\delta}\}$  [Where  $\delta$  is the deficiency of oxygen and  $x = 0, 0.10, 0.15, 0.20$ ], powders have been synthesized by sol-gel process using nitrate based powdered chemicals for SOFC applications as these powders are more useful for cathodes and anodes for SOFCs since these powders are considered to be more promising cathode materials for SOFC. Ionic conduction, Adsorption and desorption rates are the major processes that control the electrode reactions. They contribute to the overpotential. To obtain the low potential cathode materials suitable for electrolytes, Sol-Gel method is used and nano powders are prepared. The chelating agent used is Acetic acid, Ethylene glycol & Ammonia as dispersant. These powders were kept for calcinations at  $900^\circ\text{C}$  for 16 hours and at  $1050^\circ\text{C}$  for about 6 hours in crucibles of high alumina in furnace. These were characterized by XRD; SEM with EDAX, Densities, TGA, DTA, FTIR and conductivities. XRD results proved the formation of Perovskite phase at all calcination temperatures. From SEM, it is found that for some samples, there is presence of extreme porous particles in nano sizes and conductivities, densities are studied.

**Keywords:** DENSITY, XRD, SEM, SEM/EDAX, TGA/DTA, IMPEDANCE  $\{\text{Ba}_{0.5}\text{Sr}_{0.5}(\text{Co}_{0.8}\text{Fe}_{0.2})_{1-x}\text{Zr}_x\text{O}_{3-\delta}\}$

## I. INTRODUCTION

Recently strontium doped cobaltite has attracted much attention because of its mixed conduction characteristics and its relatively high ionic conductivity. Strontium doped samarium cobaltite ( $\text{SmSrCoO}$ : SSC) shows even higher conductivity, up to  $10\text{Scm}$  [13]. It shows good compatibility with ceria cathode. The cathodic reaction mechanism of SSC is not clearly understood. Ionic conduction, Adsorption and desorption rates are known as the major processes that control the electrode reactions. They contribute to the over potential. In practical the adsorption and desorption rates of SOFC are not equal. Therefore separate adsorption and desorption rates must be determined. Zhaoyu Zhong et al. (<https://doi.org/10.1016/j.ceramint.2023.11.113>) studied the High-performance  $\text{BaZr}_{0.1}\text{Ce}_{0.7}\text{Y}_{0.1}\text{Yb}_{0.1}\text{O}_{3-\delta}$  (BZCYYb) protonic ceramic fuel cell electrolytes by the Ba evaporation inhibition strategy. Their results showed that Ba evaporation inhibition strategy is proven to be an effective method to fabricate stoichiometric BZCYYb electrolytes. The content of A-site cation, Ba is strongly related to the chemical composition, grain size and electrochemical properties of the electrolyte. The main conclusions are as follows: The relative atomic ratio of Ba is normalized. BZCYYb shows a  $\text{Ba}/(\text{Zr} + \text{Ce} + \text{Y} + \text{Yb})$  of  $0.97 \pm 0.09$ , while the value of A-BZCYYb is only  $0.63 \pm 0.06$ . Out of various fuel cells, solid-oxide fuel cells (SOFCs) have the benefit of eco-friendly power generation with fuel [15] flexibility. High operating temperatures resulted in highly expensive, less compactness and low compatibility.

Hence by enhancing the porosity of cathode; one can increase the oxygen exchange and diffusion in cathode which results to higher current density in the cell. Since six years  $\text{Ba}_{0.5}\text{Sr}_{0.5}[\text{Co}_{0.8}\text{Fe}_{0.2}]_{1-x}\text{Zr}_x\text{O}_{3-\delta}$  and other combinations have got much attention for intermediate temperature of SOFCs but, this reduction in operating temperature below  $800^\circ\text{C}$  causes an increase of the over potential of SOFC cathode. Therefore, to obtain the low potential cathode materials, the material  $\text{Ba}_{0.5}\text{Sr}_{0.5}[\text{Co}_{0.8}\text{Fe}_{0.2}]_{1-x}\text{Zr}_x\text{O}_{3-\delta}$  is designed, {where 'x' is Various Compositions and 'δ' is deficiency of oxygen (0, 0.1, 0.15 and 0.20)}. By taking such doping of Zirconium with BSCF, the weight % was found to be in the present paper, the objective of the author is to prepare a cathode suitable for SOFC in single chamber fuel cell conditions. Hence, materials with a small percentage of Zr (with increasing values), BSCF samples are prepared by sol-gel method and their characterization/values are compared.

## II. EXPERIMENTAL

### A. Materials:

Commercial powders of AR grade of Aldrich Company were used in this work for the preparation of Cathode. Ethylene di-amine-tetra-acetic acid (EDTA), ethylene glycol, anhydrous citric acid, nitrate salts of Barium, Strontium, Cobalt, Iron and Zirconium oxide were purchased from Sigma Aldrich, USA. Ammonia solution is used as base. In the present observations, the Nano crystalline cathode material of  $Ba_{0.5}Sr_{0.5}[Co_{0.8}Fe_{0.2}]_{(1-x)}Zr_xO_{3-\delta}$  by varying x values, (x = 0, 0.10, 0.15, 0.20) BSCF Zr (5582Zr) powders were prepared by sol-gel process as it is one of the economical ways and characterizations like SEM/ EDAX of LEO SUPRA 55 VD ultra-high resolution of ZEISS, XRD TGA/DTA, Raman spectroscopy Impedance Analyzer were used. Barium nitrate  $Ba(NO_3)_2$ , Strontium Nitrate  $Sr(NO_3)_2$ , Cobaltous Nitrate  $Co(NO_3)_2$ , Fluka  $Fe(NO_3)_2 \cdot 9H_2O$  &  $ZrO_2$ , are used.

Flowchart of Experiment:

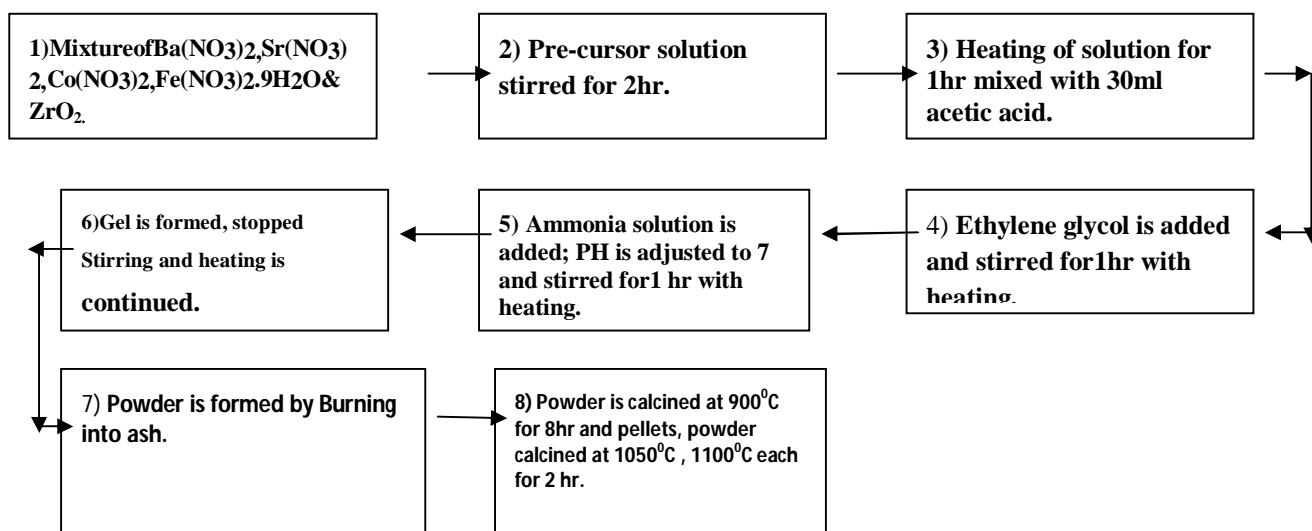


Figure: 1

### B. Method:

Precursor solution is prepared by taking above powders by appropriate formula and mixing aqueous solution of the above chemicals in molar ratio of 0.5:0.5 and 0.8:0.2 & required Acetic acid, ammonia, are added and ratio is maintained as 0.5. The solution is taken in borosil glass beaker and placed on a Magnetic stirrer with hot plate for about 4 hr with appropriate speed and by heating at about  $80^\circ C$  to  $100^\circ C$ , the solution is stirred till it becomes like a gel and then, the speed is reduced, heated for some time till it becomes ash after burning. The ash is calcined first at  $750^\circ C$ , for 8 hr, and at  $900^\circ C$ , for 8 hr and at  $1050^\circ C$ ,  $1100^\circ C$  each for 2 hr and after preparing pellets, their densities are calculated as in table.1

S.No.	Sample	Wt. in air (g)	Wt. in Xylene(g)	$\rho_{exp} = \text{Wt. in air/Loss of wt. in Xylene}$	a(Lattice constant) Å	$\rho_{th} = nM/a^3N_A$ (g/cc)	Density% = $\{\rho_{exp}/\rho_{th}\} * 100$
1.	Zr <sub>1</sub>	0.5350	0.4408	4.9161	3.99970	5.063	97
2.	Zr <sub>2</sub>	0.7266	0.5975	4.9042	4.16309	5.038	97.3
3.	Zr <sub>3</sub>	0.5954	0.4912	4.9506	4.17023	5.050	98
4.	Zr <sub>4</sub>	0.5552	0.4587	4.9749	4.19864	5.093	97.6

Table.1 Density calculations.

Sample	Cathode powder	c/n
Zr <sub>1</sub>	$Ba_{0.5}Sr_{0.5}[Co_{0.8}Fe_{0.2}]O_2$	0.5
Zr <sub>2</sub>	$Ba_{0.5}Sr_{0.5}[Co_{0.8}Fe_{0.2}]_{0.9}Zr_{0.1}O_2$	0.5
Zr <sub>3</sub>	$Ba_{0.5}Sr_{0.5}[Co_{0.8}Fe_{0.2}]_{0.85}Zr_{0.15}O_2$	0.5
Zr <sub>4</sub>	$Ba_{0.5}Sr_{0.5}[Co_{0.8}Fe_{0.2}]_{0.8}Zr_{0.20}O_2$	0.5

Table 2. Cathode BSCFZr-5582Zr) powders by sol-gel process.

### III. CHARACTERIZATION

#### A. XRD Characterization:

X-ray diffraction (XRD) analysis of the sintered samples is carried out with XRD at 40 KV and 30mA, using CuK $\alpha$  radiation with diffraction angle (2 $\theta$ ) range from 20 $^{\circ}$  to 80 $^{\circ}$  and particle size is determined by line broadening technique as shown below for all four samples. It is clear that, powder is partially amorphous and it is observed that calcined powders were of Perovskite structure and these were found to be similar with other XRD's of various authors. It is observed that, at higher temperatures, the noise in XRD is reduced. From the table 2 it is observed that as the concentration of Zr increased in B-Site of BSCF the density observed experimentally is nearly equal to the values calculated from theoretical values. The porosity values calculated for all the concentrations of Zr doped BSCF are nearly in the range of 97%. Hence, we can presume that the densification of materials is good and have the prominent role in the oxygen vacancies creation. It is also observed that the lattice constant for cubic Perovskite phase is nearly equal to all samples around the value  $a = 4.132915 \text{ \AA}$  except in the Zr<sub>1</sub> sample with small increase of  $a = \text{Å}$ . From the XRD graph for BSCFZr, 1-4 samples it is observed the cubic phase structure and the Perovskite peak for 100% intensity at around  $2\theta = 31^{\circ}$  with miller indices (110).

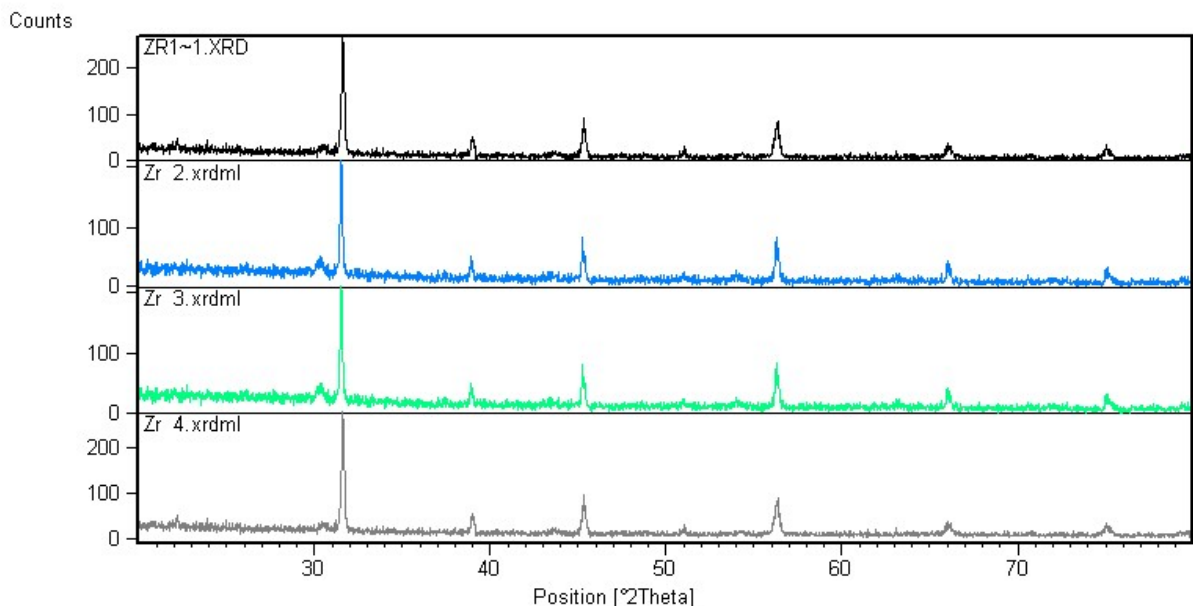


Figure.2X

RD Patterns of Ba<sub>0.5</sub> Sr<sub>0.5</sub> [Co<sub>0.8</sub>Fe<sub>0.2</sub>]<sub>1-x</sub>Zr<sub>x</sub>O<sub>3- $\delta$</sub>  with  $\delta=0$ ,  $x=0, 0.1, 0.15, 0.20$  calcined at 1050 $^{\circ}$ C.

Sample	2 $\theta$	$\theta$	Cos $\theta$	FWHM( $\beta$ )	$\beta$ Cos $\theta$	Particle size $D = \frac{0.9\lambda}{\beta \cos\theta}$
Zr 1	31.5987	17.9935	0.222	723	0.4544565	0.30509
Zr 2	17.6511	9.2555	0.816	140	0.6067302	0.228526
Zr 3	18.2550	9.275	0.733	140	0.6062206	0.228718
Zr 4	19.1931	9.655	0.50	93	0.4035698	0.343568

Table.3 XRD data for determining the average particle size of BSCFZr (5582Zr)

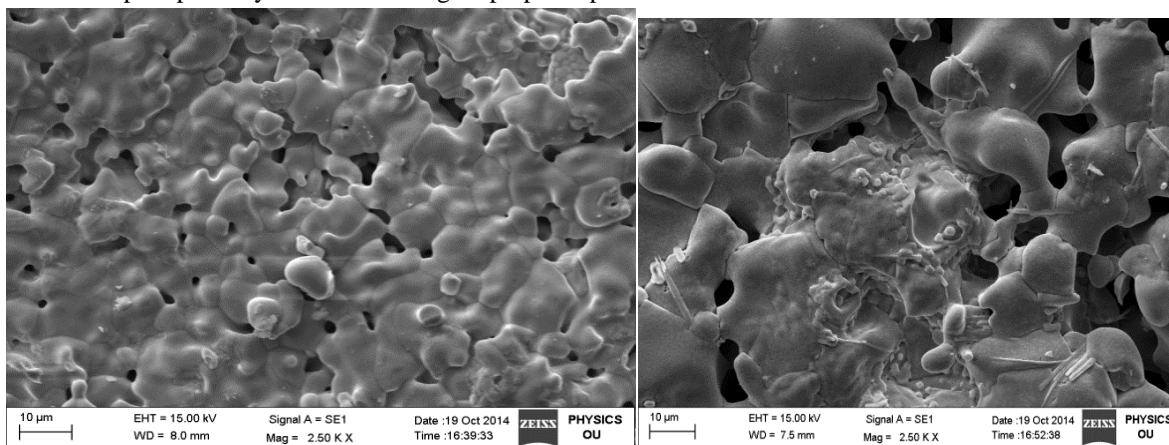
From the Table.3, It is observed that the particle size of the samples Zr<sub>2</sub> and Zr<sub>3</sub> is nearly same around 0.228622nm, while for the sample Zr<sub>4</sub> the particle size is around 0.324329nm is slightly greater than Zr<sub>1</sub> sample. That is pure BSCF sample. It is also observed that there is a variation in FWHM values.

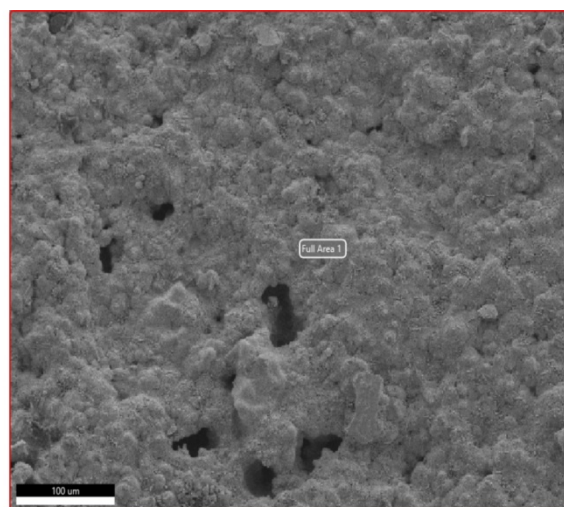
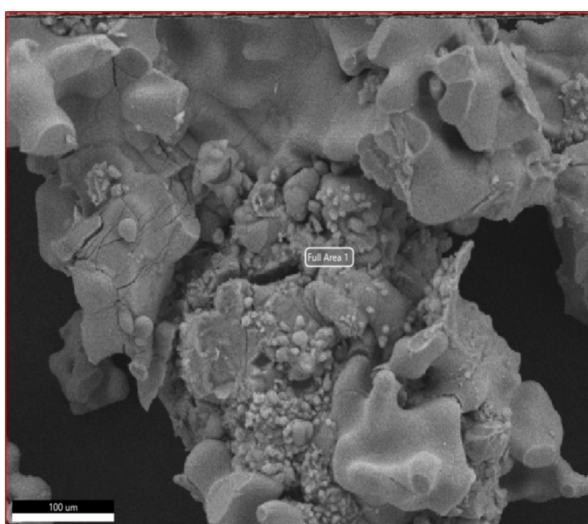
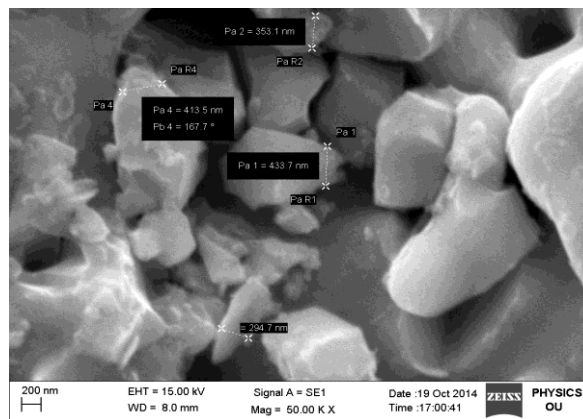
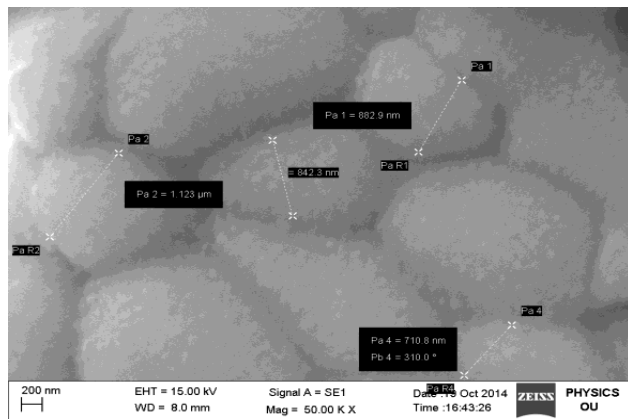
From the above data, the percentage density of the samples increased as partial substitution of lighter elements with heavier element increases due to the concentration of dopant Zr on B-site. As a result, the porosity of samples decreases by small amount due to dopant concentration. Even if porosity is one of the key criteria for SOFC cathode materials, stability of material also plays a great role on the performances of SOFCs. The stability depends on the crystalline of material and it was observed that the crystalline nature of the samples increased as the concentration of fifth dopant on B-site increases. But the porosity of samples was not decreased that much due to the increment of dopant concentration.

Therefore, doping of fifth element on B-site had great positive influence on the performance of these SOFC cathode materials. The variation of parameters more likely a compensatory response of the crystal structure to accommodate dopants of different ionic size as compared to those of host ions which causes the shrinkage of crystal lattice that leads to decrease in the values of lattice constants and cell volume (V). The observed increase in the value of percentage density with the incorporation of dopant ions for all synthesized series is due to (i) Larger molar mass of doped metal cations compare to that of host pair i.e. (CoFe)- Zr and (ii) shrinkage of lattice that leads to the observed decrease in the value of V. The results of average crystallite size of nano particles and lattice parameters are summarized in Table 2. As it is seen from the data, position of the highest intensity peak is displaced a small amount to the high angle due to the concentration of dopant element Zr on B-site. The plane giving rise to the smallest Bragg angle would have the highest d-spacing. Average crystallite size, lattice parameter and cell volume also decreases with the increment of fifth dopant on B-site due to the shifting of position angle which leads to the decrement of d-spacing. As we have observed from the Table 3, crystalline nature of the prepared materials increased as the concentration of fifth dopant zirconium increases. This is proved by seeing the values of intensity peaks. The value of intensity peaks increased more as the concentration of fifth dopant Zr increased.

### B. SCANNING ELECTRON MICROSCOPY (SEM)

Scanning electron microscopy (SEM) is applied to investigate the morphology of samples prepared in this work. By using a high resolution SEM, the structural properties of the synthesized pellets were analyzed and related them with physical behavior of the particles as a cathode material. All samples were analyzed by high resolution SEM micrographs to know the densification of BSCFZ synthesized by sol-gel technique to be used as intermediate temperature cathode materials. The obtained images from SEM represent the variation in intensity of the signal collected by the detector as a function of X- Y space on the specimens. SEM Images are in fact two-dimensional representations of three-dimensional objects. However, the high depth of field SEM lend three dimensional appearances to the specimen images. Among the various interactions, secondary and backscattered electrons are generally utilized for micro structural investigations, since their intensities vary sensitively with surface topography, a high resolution SEM (ZEISS) was used to see the morphology of synthesized samples and to relate them with physical behaviors of the particles used as a cathode material. In the present study SEM analysis was carried out by using the sintered pellets of the samples. SEM analysis is considered “non-destructive”, i.e., X-rays produced by electron interactions do not lead to loss of sample volume, making it possible to analyze the same sample repeatedly without affecting the prepared pellets.





Figures 3a, 3b, 3c, 3d, 3e, 3f

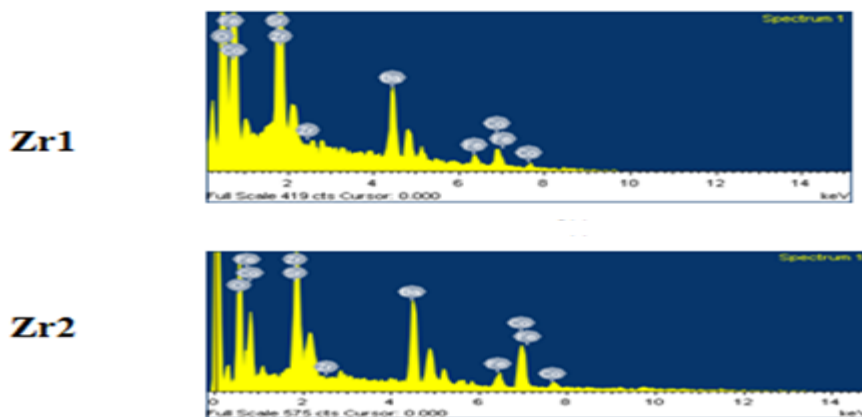
As it is clearly seen from Figure, the crystal consists of a periodic arrangement of the unit cell into a lattice. The unit cell can contain a single or more atoms in a fixed arrangement. SEM micrograph clearly shows the presence of uniform grains with clean and distinct grain boundaries. It exhibited complete densification with a presence of pores on the surface. Grain boundaries are visible and the grain sizes are clearly increased. The average grain size of the sample found from SEM image was 373.5 nm. Increasing the sintering temperature leads to complete densification and posterior grain growth and force all metals into the crystal network. The porosity has increased over the sample before debinding and sintering because the loss of binding agents used accounts for the increased porosity. Decreasing of sample porosity is due to the increases of sintering temperatures used. This additional sintering has partially counteracted the pore-forming effect of removing the binding agents (Pike, 2015). Figures 3a, 3b, 3c, 3d, 3e, 3f shows SEM micrograph of the prepared sample for cathode material  $\text{Ba}_{0.5}\text{Sr}_{0.5}(\text{Co}_{0.8}\text{Fe}_{0.2})_{1-x}\text{Zr}_x\text{O}_{3-\delta}$  ( $x=0.1$ ) with high resolution at a magnification of 200 nm. Using a high sintering temperature helps to transform the material from purely amorphous into a weakly crystalline structure. SEM micrograph clearly shows the presence of uniform grains with clean and distinct grain boundaries. It exhibited complete densification with a presence of pores on the surface. Grain boundaries are visible and the grain sizes are clearly increased. The average grain size of the sample found from SEM image was 373.5 nm. Even though the microstructure does not appear to be a perfect Perovskite network due to some impurities in the sample, we got a perfect BSCFZP Perovskite by using very high sintering temperature between (900°C and 1100°C). Figures above shows a high resolution SEM micrograph of the prepared sample for  $\text{Ba}_{0.5}\text{Sr}_{0.5}(\text{Co}_{0.8}\text{Fe}_{0.2})_{1-x}\text{Zr}_x\text{O}_{3-\delta}$  ( $x=0.15$ ) at a magnification of 200 nm.

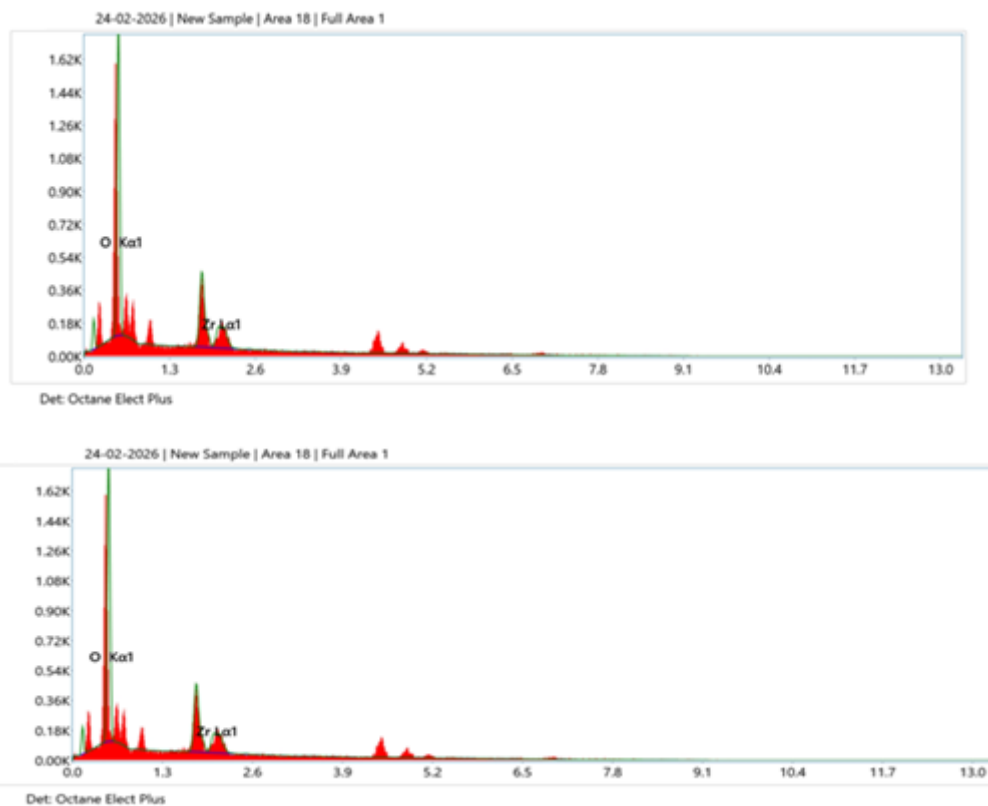
As it can be seen from the figure, particle size was in nanometer range which means that high temperature and concentrations of Zr doping lead to grain growth. It exhibited complete densification with presence of pores on the surface. Grain boundaries are visible and the grain sizes are clearly increased. The average grain size of the sample found from SEM image was 373.5 nm. The average grain size is decreased and shows the sample was more stabilized.

Figure above shows a high resolution SEM micrograph of the prepared sample for  $Ba_{0.5}Sr_{0.5}(C_{0.8}Fe_{0.2})_{1-x}Zr_xO_{3-\delta}(x=0.2)$  at a magnification of 200 nm. As it is visible at higher magnifications, the crystallinity seems to get more established rather than previous samples. Particle size was still in nanometer range. It exhibited complete densification with presence of pores on the surface. Grain boundaries are visible and the grain sizes are clearly shown. As thermogravimetric results demonstrate higher temperatures are necessary for complete degradation of impurities and the sintering process at high temperature leads to the formation of a secondary phase at the surface. Average grain sizes of the sample found from SEM image were 373.5 nm. Crystals consist of planes of atoms that are spaced distance 'd' apart which can be resolved into many atomic planes each with a different 'd' spacing, a, and b (length). The angles between a, b and c (but for cubic phase a=b=c) are lattice constants or parameters which can be determined by XRD termed as grain structures and the region where by each unit cell separated were grain boundary. When the sintering process takes place due to the difference in lattice parameters arrangement for the cubic phase of BSCFZr the holes are formed. In general, it is evident that the majority of synthesized samples are spherical with a uniform surface morphology. The surfaces of synthesized samples exhibit well defined crystalline nano particles. Few of them are formed as agglomerates of smaller particles and appeared as lumps. The grain growth of such agglomerates on the surface is however, normal. The individual nanoparticles may tend to coalesce together due to sintering of the samples at high temperatures of 950 °C during synthesis. The average grain sizes in each of the synthesized series, get smaller when the dopant content increases as also evident from XRD data. Further reduction in average grain sizes of particles for doped samples as compared to undoped sample is owing to the incorporation of co-dopants in Perovskite cathodes and it is in the range of 350 nm. In this study, average grain size of all the samples was calculated by linear intercept technique. The findings obtained are more porous than previous literature that were around 5% (Sharma & Rao, 2015).

### C. SEM with EDAX:

From SEM with EDAX analysis, it is found that the atomic percentage as taken in the formula is not changed and all atoms are present in the same proportion, particle sizes are noted which are in good coincidence with the data taken from XRD. The figures 4a, 4b, 4c, 4d, 4e and 4f show the presence of Ba, Sr, Co, Fe, Zr peaks. The appearance of c may be due to usage of acetic acid. This C % has been reduced by calcining the samples at a higher temperature. From the results of energy dispersive x-rays spectroscopy (EDS) analysis obtained, all the samples had the required elemental composition with their proportional weight and atomic percentage as shown in Figure above. As we can have observed from Figure above the energy dispersive x-rays spectroscopy (EDS) graphs confirmed the presence of elements Ba, Sr, Co, Fe, Zr, O in the prepared samples and no other elements were observed. Elemental compositions of some representative samples of each synthesized series with composition revealed that the elemental compositions of the samples are in conformity to their nominal stoichiometry as shown in Table above.





Figures 4a, 4b, 4c, 4d

**D. TGA/DTA CHARACTERIZATION:**

**1) Introduction**

Thermo gravimetric Analysis (TGA) and Differential Thermal Analysis (DTA) are used to study the thermal stability and decomposition behavior of materials. This report presents the analysis of two samples: Zr<sub>1</sub> and Zr<sub>2</sub>.

The curves in figures 5(a) and 5(b) correspond to TGA (weight loss in % Vs temperature) and DTA (Rate of losing weight Vs temperature) for Ti<sub>1</sub> and Ti<sub>2</sub> samples. DTA is studied with difference in temperature and flow of heat between the sample and a reference. Moisture, Thermal stability and composition are studied simultaneously by TG/DTA referring Exothermic and Endothermic processes.

Powder samples of **Zr1** of 8.3mg and **Zr2** of 10.9mg are taken and corresponding curves are recorded. The weight loss is observed for three times in TGA first at 120<sup>0</sup>C due to evaporation of moisture, second at 400<sup>0</sup>C due to evaporation of nitrates and third at 650<sup>0</sup>C due to evaporation of other impurities because of usage of acids, bases etc.,. The melting point can be at about 1100<sup>0</sup>C. TGA-DTA is performed to determine changes in weight in relation to change in temperature. Such analysis relies on a high degree of precision weight, temperature and temperature change. All precursor samples are placed on the platinum pan that is suspended from the analytical balance located outside the furnace chamber of the instrument TGA Q500V20.13 Build 39. The balance is zeroed and the sample cup is heated up from room temperature to 800<sup>0</sup>C. Powders of 8.3mg, 10.9mg were taken and corresponding curves were recorded for **Ba<sub>0.5</sub>Sr<sub>0.5</sub>(CO<sub>0.8</sub>Fe<sub>0.2</sub>)<sub>x</sub>O<sub>3-δ</sub>** (1-x)

**Zr<sub>x</sub>O<sub>3-δ</sub>** at x=0, 0.1, 0.15 & 0.2 respectively. The TGA curve calculations of all samples on this study indicated that the decomposition of calcite occurred at lower temperature. The decompositions of nitrates affected by the amount of NO<sub>2</sub> gas present during firing. As (Sharma & Rao, 2015) stated, the weight loss is observed three times in the curve. First it was due to evaporation of moisture, second due to evaporation of nitrates and the third due to evaporation of other impurities that comes from the usage of acids and bases. All samples displayed a very slight increase in the rate of expansion above 800<sup>0</sup>C which maybe attributed to the loss of oxygen leading to the reduction (and subsequent increase in radius) of the Co/Fe on the B site. However, this increase in expansion rate is small, suggesting limited reduction in air.

The curves in Figures 5a, 5b represent TGA (weight loss in percent vs. temperature) and DTA (rate of losing weight vs. temperature) for  $\text{Ba}_{0.5}\text{Sr}_{0.5}(\text{CO}_{0.8}\text{Fe}_{0.2})_{(1-x)}\text{Zr}_x\text{O}_{3-\delta}$  samples at  $x=0, 0.1, 0.15$  and  $0.2$  respectively. As it is observed from Figures 5a, 5b, there were weight losses observed three times in the curve for the prepared sample at a concentration of  $x=0$  which is there is no doping of titanium on B-site. The first weight loss was around  $120^\circ\text{C}$  due to evaporation of moisture, the second weight loss was around  $400^\circ\text{C}$  due to evaporation of nitrates and the third weight loss was around  $650^\circ\text{C}$  due to evaporation of other impurities that comes from the usage of acids and bases. This result tells information about the sintering temperatures at which the prepared sample must be sintered. As we have observed from Figures 5(a), 5(b), due to evaporation of other impurities that comes from the usage of acids and bases. This result tells information about the sintering temperatures at which the prepared sample must be calcined and sintered.

From the results obtained, information about the sintering temperatures at which the prepared sample must be sintered was taken. As it is seen from the curves for all samples, there was a more intense degradation of nitrates at lower temperatures. But mass loss is not stabilized perfectly at  $800^\circ\text{C}$ . This might indicate that there were a few intermediate compounds to be decomposed. This tells an information about the sintering temperatures must be larger than  $800^\circ\text{C}$  to decompose all the compounds and remove the impurities from samples completely.

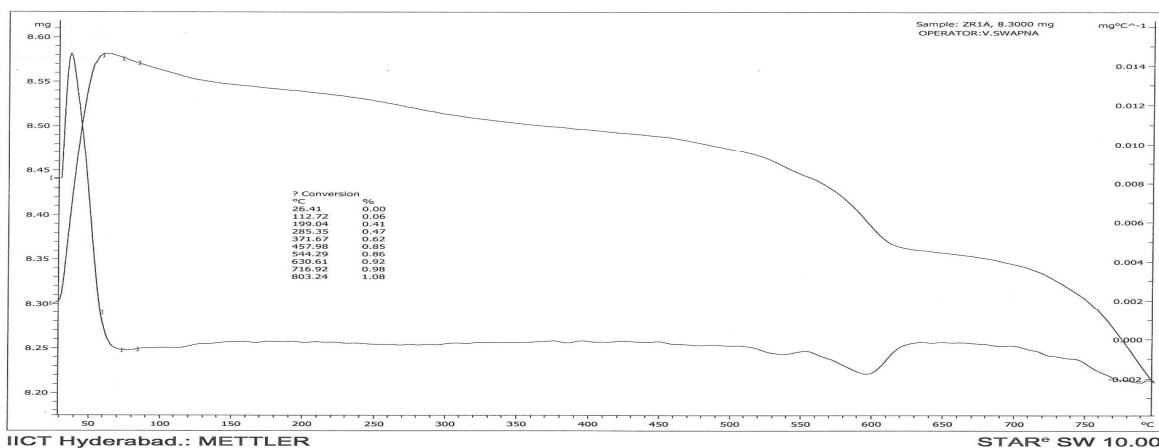


Figure 5(a) TGA/DTA Curves for  $\text{Ba}_{0.5}\text{Sr}_{0.5}[\text{Co}_{0.8}\text{Fe}_{0.2}]_{0.9}\text{Zr}_{0.1}\text{O}_2$   
Temperature (X-Axis), Weight loss in % (Y-Axis)

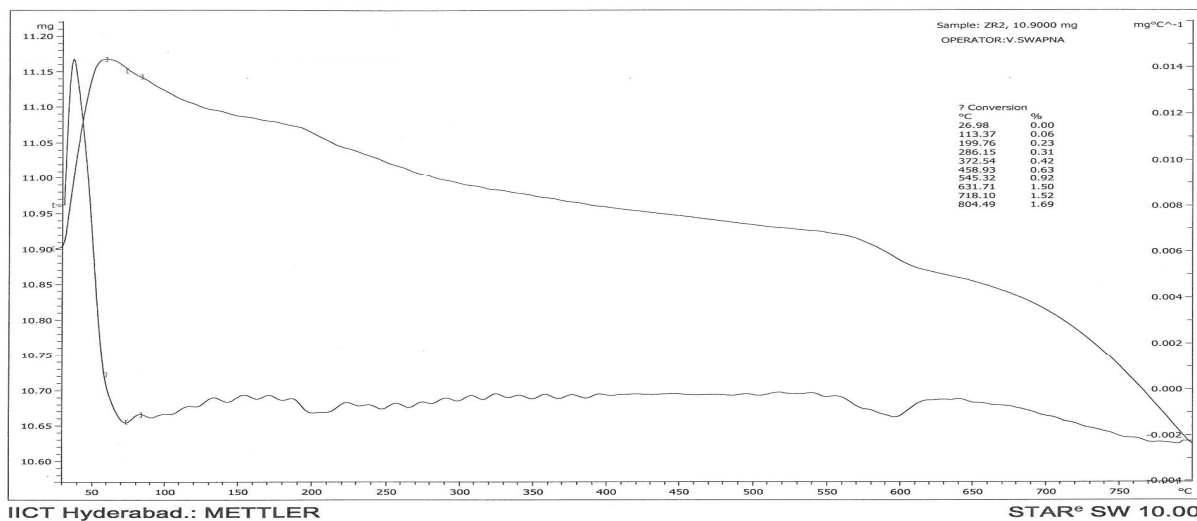


Figure 5(b) TGA/DTA Curves for  $\text{Ba}_{0.5}\text{Sr}_{0.5}[\text{Co}_{0.8}\text{Fe}_{0.2}]_{0.85}\text{Zr}_{0.15}\text{O}_2$   
Temperature (X-Axis), Weight loss in % (Y-Axis)

2) Sample Details

Sample	Initial Mass (mg)	Final Mass (mg)
Zr <sub>1</sub>	8.30	8.20
Zr <sub>2</sub>	10.90	10.63

Table(4)

3) Analysis of Sample Zr<sub>1</sub>

Total Weight Loss: ~1.08%

Stages of Decomposition:

- 30–120°C: Moisture removal
- 120–400°C: Loss of volatile components
- 400–650°C: Structural changes
- 650–800°C: Final decomposition

DTA Observations:

- Small endothermic peak around 600°C
- No strong exothermic reactions.

4) Analysis of Sample Zr<sub>2</sub>

Total Weight Loss: ~1.69%

Stages of Decomposition:

- 30–120°C: Moisture removal
- 120–400°C: Volatile loss
- 400–650°C: Pronounced decomposition
- 650–800°C: Final degradation

DTA Observations:

- Stronger endothermic peak near 600°C
- Minor fluctuations indicating structural changes.

5) Comparison of Zr<sub>1</sub> and Zr<sub>2</sub>

Property	Zr <sub>1</sub>	Zr <sub>2</sub>
Total Weight Loss	~1.08%	~1.69%
Thermal Stability	Higher	Lower
DTA Peak Intensity	Mild	Stronger
High Temperature Behavior	Stable	More reactive

Table(5)

6) Conclusion

Both samples exhibit high thermal stability with minimal weight loss. Sample Zr<sub>1</sub> shows better stability compared to Zr<sub>2</sub>. Zr<sub>2</sub> exhibits slightly higher decomposition and stronger thermal activity.

E. Fourier Transform Infrared (FTIR) spectroscopy:

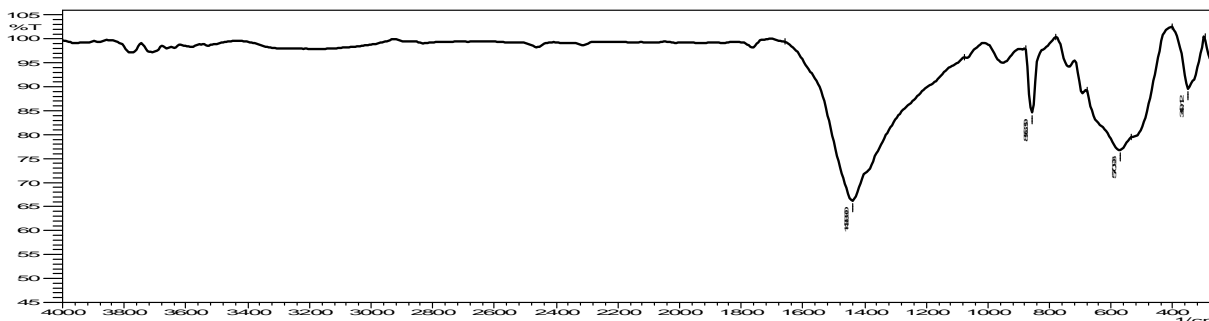


Figure.6 (a)

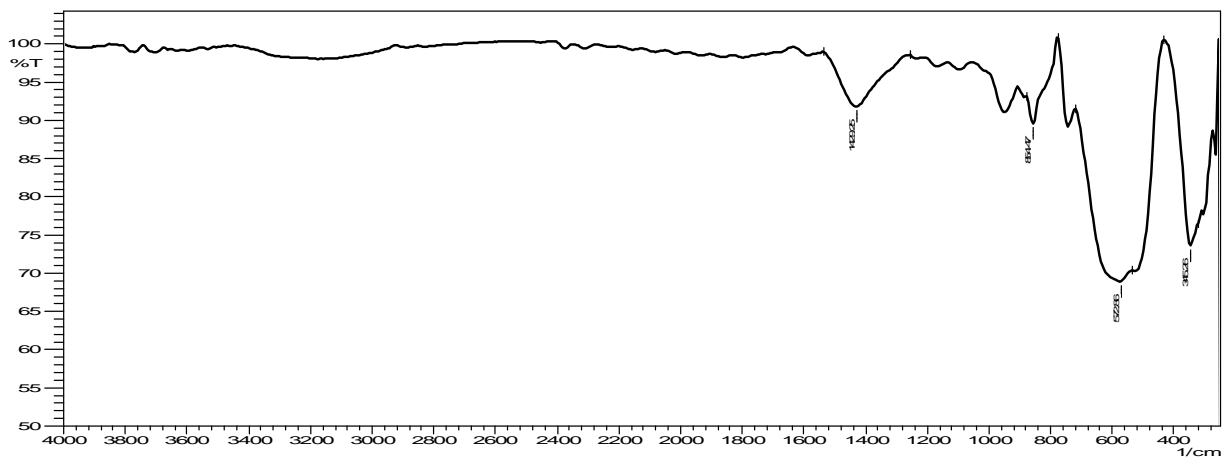


Figure.6 (b)

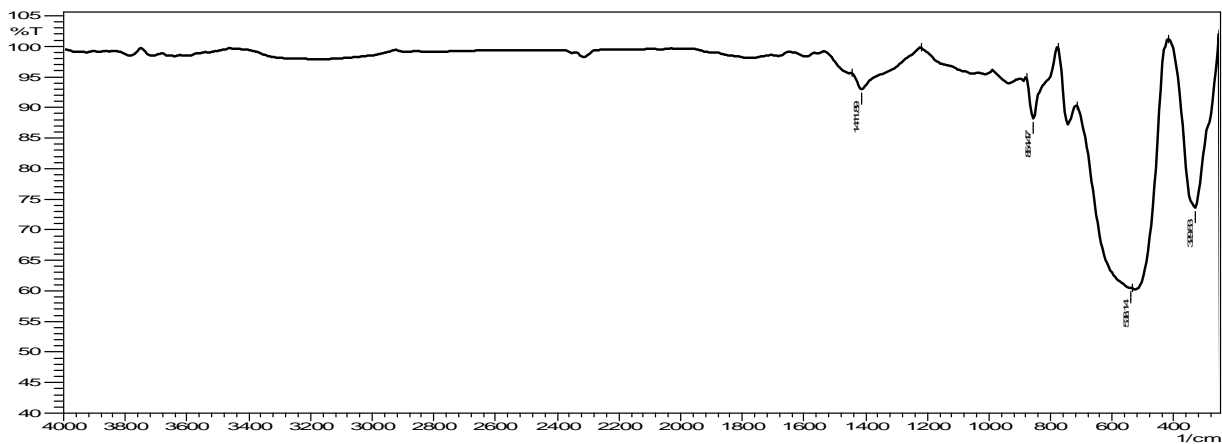


Figure.6 (c)

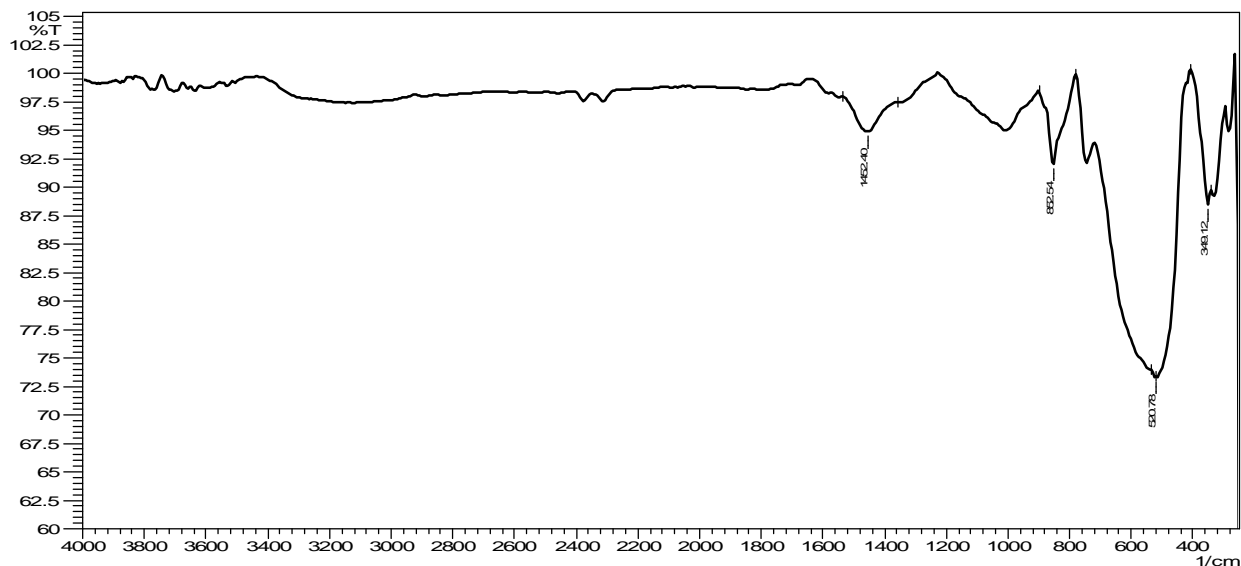


Figure.6 (d)

FTIR Analysis Report of Zirconium Oxide Samples

Four samples (Zr<sub>1</sub>, Zr<sub>2</sub>, Zr<sub>3</sub>, and Zr<sub>4</sub>) were analyzed using FTIR spectroscopy to study functional groups and bonding characteristics.

a) Common Observations

Broad peak ~3400–3200 cm<sup>-1</sup> indicates O–H stretching (adsorbed water). Peaks ~1600–1400 cm<sup>-1</sup> indicate H–O–H bending or carbonate traces. Strong peaks below 800 cm<sup>-1</sup> correspond to Zr–O and Zr–O–Zr vibrations.

b) Sample-wise Analysis

**Zr<sub>1</sub>**

- 1438 cm<sup>-1</sup>: O–H bending
- 856 cm<sup>-1</sup>: Zr–O
- 570 cm<sup>-1</sup>: Zr–O–Zr
- 349 cm<sup>-1</sup>: lattice vibration

**Zr<sub>2</sub>**

- 1421 cm<sup>-1</sup>: O–H bending
- 860 cm<sup>-1</sup>: Zr–O
- 621 cm<sup>-1</sup>: Zr–O–Zr
- 345 cm<sup>-1</sup>: lattice vibration

**Zr<sub>3</sub>**

- 1411 cm<sup>-1</sup>: O–H bending
- 854 cm<sup>-1</sup>: Zr–O
- 538 cm<sup>-1</sup>: Zr–O–Zr
- 329 cm<sup>-1</sup>: lattice vibration

**Zr<sub>4</sub>**

- 1452 cm<sup>-1</sup>: O–H bending
- 852 cm<sup>-1</sup>: Zr–O
- 520 cm<sup>-1</sup>: Zr–O–Zr
- 349 cm<sup>-1</sup>: lattice vibration

S.No.	Sample	Hydroxyl Content	Crystallinity	Structural Order
1.	Zr <sub>1</sub>	Lowest	Highest	Best
2.	Zr <sub>2</sub>	High	Low	Moderate
3.	Zr <sub>3</sub>	Moderate	Medium	Improved
4.	Zr <sub>4</sub>	Lower	Higher	Good

Table 6 –Comparative table

Conclusion

All samples confirm zirconium oxide formation. From Zr<sub>1</sub> to Zr<sub>4</sub>, hydroxyl content decreases while crystallinity and structural stability increase. Zr<sub>1</sub> shows the most well-defined oxide structure.

F. Impedance:

To characterize the electrochemical properties of BSCFZ cathode, AC impedance values are measured and characterization of cathode processes is based on the application of ac potential

$$E(t) = E_0 \cos(\omega t + \phi) \text{ ----- (1)}$$

$$\text{of minimum amplitude such that ac current } I(t) = I_0 \cos(\omega t - \phi) \text{ ----- (2)}$$

is obtained. Impedance,  $Z = \text{----- (3)}$  is calculated at different AC frequencies up to few MHz. The impedance measurements characterizes the physical and chemical processes related to time constants, electron transfer at high frequencies and mass transfer at low frequencies.

In the present study, the impedance measurements were carried from room temperature to 150<sup>0</sup> C and NY  
 Quist plots ( $Z_s = Z_{Real} + Z_{Imaginary}$ ) are drawn as shown in figures a& b  
 The cole-cole plots are observed for  $Z^I$  and  $Z^{II}$  plots are as depicted in figures a & b  
 AC conductivity is calculated by the formula  $\sigma_{ac} = \frac{Y^I t}{A}$  where  $Y^I$  is called admittance, t is thickness of the sample and A is area of the sample. The conductivities are tabulated in tables 2 & 3 below.

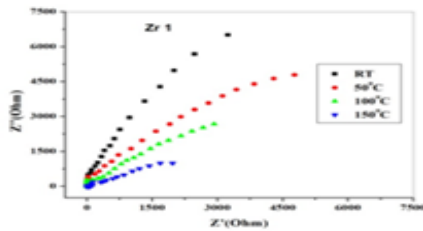


Fig. 7(a)  $Z^I$  Vs  $Z^{II}$  of  $Zr_1$  Sample

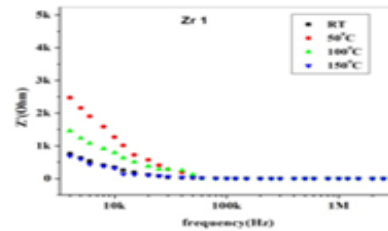


Fig 7(b) Frequency Vs  $Z^I$  of  $Zr_1$  Sample

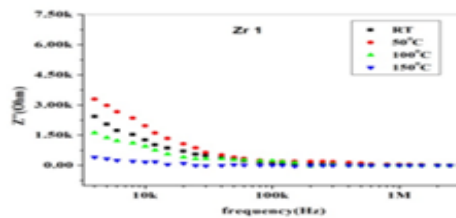


Fig. 7(c)  $Z^I$  Vs  $Z^{II}$  of  $Zr_1$  Sample

Figure.7

S.No	Temperature	Resistance (ohm)	Admittance(Y)	Area(A)m <sup>2</sup>	Thickness(t)m	$\sigma_{ac} = \frac{Y^I t}{A}$ S / m
1	Roomtemp.	1550	$4.925 \times 10^{-4}$	$69.42 \times 10^{-6}$	$1.46 \times 10^{-3}$	$1.04 \times 10^{-2}$
2	50	1125	$9.33 \times 10^{-4}$	$69.42 \times 10^{-6}$	$1.46 \times 10^{-3}$	$1.96 \times 10^{-2}$
3	100	486	$1.92 \times 10^{-3}$	$69.42 \times 10^{-6}$	$1.46 \times 10^{-3}$	$4.04 \times 10^{-2}$
4	150	198	$3.45 \times 10^{-3}$	$69.42 \times 10^{-6}$	$1.46 \times 10^{-3}$	$7.26 \times 10^{-2}$

Table6. Calculation of conductivities of  $Zr_1$  Sample

S.No	Temperature	Resistance	Admittance	Area(A)m <sup>2</sup>	Thickness(t)m	$\sigma_{ac} = \frac{Y^I t}{A}$ S / m
1	Roomtemp.	380	$2.185 \times 10^{-3}$	$70.6124 \times 10^{-6}$	$1.42 \times 10^{-3}$	$4.39 \times 10^{-2}$
2	50	290	$4.186 \times 10^{-3}$	$70.6124 \times 10^{-6}$	$1.42 \times 10^{-3}$	$8.42 \times 10^{-2}$
3	100	105	0.01235	$70.6124 \times 10^{-6}$	$1.42 \times 10^{-3}$	$2.48 \times 10^{-1}$
4	150	62	0.02	$70.6124 \times 10^{-6}$	$1.42 \times 10^{-3}$	$4.02 \times 10^{-1}$

Table7. Calculation of conductivities of  $Zr_2$  Sample

From the tables, it is observed that as the temperature is increased the from rt to 150<sup>0</sup>C the resistance of the all samples of BSCFZ1-4 decreased and subsequently conductivity increased in the order of ten times from 0.062 -0. 402. Further increase of temperature the resistance drops abnormal and electronic conductivity dominates, the ionic conductivity. In the contribution of total conductivity of samples. In general in perovskite samples most of them are ceramic nature the ionic conductivity contribute more at high temperature around 600<sup>0</sup>C. Since BSCFZ samples contain metal ions, so electronic conductivity more rather than ionic conductivity, So to increase ceramic nature and improve ionic conductivity, the slight doping of Zr in the place of Fe, Co in the B- site of perovskite results the increase of ionic conductivity.

As the concentration of Zr slightly increased in BSCFZr the resistance is decreased and ac conductivity is increased as 0.084 to 0.402.s/m.

The Zr moderate doping in BSCFO cathodes will maintain phase stability (perovskite cubic) of the samples which observed in DTA-TGA experiment results the enhancement of diffusion pathways and results the increase of ionic conductivity in all samples. The major contribution for the conductivity is creation of oxygen vacancies which helps the oxygen ion migration from cathode to anode through electrolytes in SOFC.

Ionic conductivity in BSCF depends on oxygen vacancies ( $V_{O''}$ ) which explained by koger-vink relations. Moderate doping of Zr can stabilize oxygen vacancies and maintain mixed ionic and electronic conductivity in BSCFZr sample. The activation energies also for oxygen diffusion will maintain moderate and reach near to level of oxygen ions.

#### IV. CONCLUSION

The moderate doping of Zr in BaSrCoFeO<sub>3</sub> cathodes has improved the ionic conductivity at high temperatures by stabilizing the cubic perovskite structure indirectly by optimizing the oxygen vacancy distribution, enhancing oxygen diffusion pathways. It also reduced the Co/Fe redox activity can limit the charge compensation and promising materials for mixed ionic electronic conductivity in cathodes of IT-SOFC.

#### REFERENCES

- [1] T. Ishihara, H. Matsuda, Y. Takita, J. Am. Chem. Soc. 116(1994) 3801
- [2] K. Huang, M. Feng, J.B. Goodenough, J. Electrochem. Soc.
- [3] J.P.P. Huijismans, F.P.F. Berkel, G.M. Christie, J. Power
- [4] R. Maric, S. Ohara, T. Fukui, H. Yoshida, M. Nishimura, T. Vol. PV 94-12, Electrochemistry Society, 1994, Inagaki, K. Miura, J. Electrochem. Soc. 146 2006
- [5] P. Huang, A. Horkas, A. Petric, J. Am. Ceram. Soc. 82 (1999) Electrochem. Soc. 134 (1978) 21412402
- [6] F. Chen, M. Liu, J. Solid State Electrochem. 3 (1998) 7. Tuller (Eds) Proceeding 1st International Symposium Ionic
- [7] T. Ishihara, H. Matsuda, Y. Takita, in: Proceedings 2nd Ionic and Mixed Conducting Ceramics, Electrochemistry Society, and Mixed Conducting Ceramics, Vol PV 94-12, Electro- 1991, p. 122. Chemistry Society, 1994, p. 85.
- [8] T. Ishihara, M. Honda, Y. Takita, Recent Res. Dev. Electrochem 2 (1999) 15
- [9] N.Q. Minh, T. Takahashi, in: Science and Technology of Nishiguchi, Y. Takita, J. Electrochem. Soc. 145 (1999) 3177. Ceramic Fuel Cell, 1995, p. 147.
- [10] S. Majumdar, T. Claar, B. Flandermeyer, J. Am. Ceram. Soc. 144 (1997) 3620. 69
- [11] O. Yamamoto, Y. Takeda, R. Kanno, H.U. Anderson, Solid State Ionics 22 (1989)
- [12] A. Hammouche, E. Siebert, A. Hammou, Mater. Res. Bull. 24 (1989) 367.
- [13] T. Ishihara, M. Honda, T. Shibayama, H. Minami, H. Nishiguchi, Y. Takita,
- [14] J. A. Kilner, R.A. De Souza, I. C. Fullarton, Solid state Ionics P. SSC 86-88 (1996) 703. O2
- [15] A Boudghene Stambouli and E. Traversa, Renewable and Suitable Energy Rev., 6.433 (2002)
- [16] S. J. Skinner, Jnt. T. Inorganic Matter., 3, 113 (2001)
- [17] Z. Shao and S. M. Haile, Nature (London) 431, 432, 170 (2004)
- [18] Y. Itoh V, Nishida, A. Tomita, Y. Fujie. Solid state communication. 149. 41 (2008)
- [19] B. Liu, Y. Zhang and L. Tang, Int. J. Hydrogen Energy, 34, 435 (2009)
- [20] X. Sun, S. Li, J. Sun, X. Liu, B. Zhu, Int. J. Electrochem. Sci. (2007) 462
- [21] A. Subrahmania, T. Saradha, S. Muzumathi, J. Power Sources 165 (2007) 728
- [22] H. Zhao, F. Mauvy, C. Lalanne, J.M. Bassat, S. Fourcade, J.C Grenier, Solid State Ionics 179 (2008) 2000
- [23] A. Princivalle, E. D. Jurado, SSI 179 (2008) 1921
- [24] V. B. Vert, J.M. Serra, Fuel Cells (2009) 663
- [25] Y. Li, R. Gemmen, X. Liu, J. Power sources, 195 (2010) 3345 [26] S.S. Shimizu, T. Yamaguchi, Y. Fujishiro, ECS Tans. 25 (2009) 975
- [26] Ionic transport modification in proton conducting BaCe<sub>0.6</sub>Zr<sub>0.3</sub>Y<sub>0.1</sub>O<sub>3-δ</sub> with transition Metal oxide dopants Solid State Ionics (2016) C. Jin
- [27] Effect of Ba nonstoichiometry on the phase composition, microstructure, chemical stability and electrical conductivity of Ba<sub>x</sub>Ce<sub>0.7</sub>Zr<sub>0.1</sub>Y<sub>0.1</sub>O<sub>3-δ</sub> (0.9 ≤ x ≤ 1.1) proton conductors. Ceram. Int. (2015) Y. Liu
- [28] Enhanced sinter ability of BaZr<sub>0.1</sub>Ce<sub>0.7</sub>Y<sub>0.1</sub>O<sub>3-δ</sub> by addition of nickel oxide J. Power Sources (2011) H.-I. Ji
- [29] Influence of sintering activator on electrical property of BaZr<sub>0.85</sub>Y<sub>0.15</sub>O<sub>3-δ</sub> proton-conducting electrolyte J. Power Sources (2021) L. Mahmud et al.
- [30] Challenges in fabricating planar solid oxide fuel cells: a review Renew. Sustain. Energy Rev. (2017) U. Damo et al.
- [31] Solid oxide fuel cell hybrid system: a detailed review of an environmentally clean and efficient source of energy (2019) D. Guo et al.
- [32] Preparation and characterization of highly active and stable NdBaCo<sub>0.8</sub>Fe<sub>0.8</sub>Ni<sub>0.4</sub>O<sub>5+δ</sub> oxygen electrode for solid oxide fuel cells Electrochim. Acta (2023) M. Jafari et al.
- [33] Enhancement of an it-sofc cathode by introducing ysz: Electrical and electrochemical properties of la<sub>0.6</sub>ca<sub>0.4</sub>fe<sub>0.8</sub>ni<sub>0.2</sub>o<sub>3-δ</sub>-ysz composites Int. J. Hydrog. Energy (2019) C.W. Chen et al.
- [34] Electrochemical performance of lanthanum calcium cobalt ferrite cathode interfaced to lamox electrolyte Solid State Ion. (2008) K. Efimov et al.
- [35] Ca-containing co<sub>2</sub>-tolerant perovskite materials for oxygen separation J. Membr. Sci. (2012) M. Salehi et al.
- [36] Oxygen permeation and stability study of (la<sub>0.6</sub>ca<sub>0.4</sub>)<sub>0.98</sub>(co<sub>0.8</sub>fe<sub>0.2</sub>)<sub>0.3</sub>o<sub>3-δ</sub> membranes J. Membr. Sci. (2017) Z. Pan et al.

- [37] Study of activation effect of anodic current on  $\text{La}_{0.6}\text{Sr}_{0.4}\text{Co}_{0.2}\text{Fe}_{0.8}\text{O}_{3-\delta}$  air electrode in solid oxide electrolyzer cell *Electrochim. Acta* (2016) A.I. Klyndyuk et al.
- [38] Double substituted  $\text{NdBa}(\text{Fe}, \text{Co}, \text{Cu})_{2}\text{O}_{5+\delta}$  layered perovskites as cathode materials for intermediate-temperature solid oxide fuel cells—correlation between structure and electrochemical properties *Electrochim. Acta* (2022) A. Mroziński et al.
- [39] Electrochemical properties of porous  $\text{Sr}_{0.86}\text{Ti}_{0.65}\text{Fe}_{0.35}\text{O}_3$  oxygen electrodes in solid oxide cells: Impedance study of symmetrical electrodes *Int. J. Hydrog. Energy* (2019)
- [40] S. Dwivedi Solid oxide fuel cell: materials for anode, cathode and electrolyte *J. Hydrog. Energy* (2020) P. Kaur et al.
- [41] Review of perovskite-structure related cathode materials for solid oxide fuel cells *Ceram. Int.* (2020) N. Mahato et al.
- [42] Progress in materials science Progress in material selection for solid oxide fuel cell technology : A review *Prog. Mater. Sci.* (2015) M. Liang et al.
- [43] Nickel-doped  $\text{BaCo}_{0.4}\text{Fe}_{0.4}\text{Zr}_{0.1}\text{Y}_{0.1}\text{O}_{3-\delta}$  as a new high-performance cathode for both oxygen-ion and proton conducting fuel cells *Chem. Eng. J.* (2021) Y. Yamaguchi et al.
- [44]  $\text{La}_{0.65}\text{Ca}_{0.35}\text{FeO}_{3-\delta}$  as a novel Sr- and Co-free cathode material for solid oxide fuel cells *J. Power Sources* (2020) L. Zhan et al.  $\text{BaCo}_{0.4}\text{Fe}_{0.4}\text{Zr}_{0.2}\text{O}_{3-\delta}$ : evaluation as a cathode for ceria-based electrolyte IT-SOFCs *J. Alloys Compd.* (2019) H.Y. Tu et al.
- [45]  $\text{Ln}_{0.4}\text{Sr}_{0.6}\text{Co}_{0.8}\text{Fe}_{0.2}\text{O}_{3-\delta}$  ( $\text{Ln}=\text{La}, \text{Pr}, \text{Nd}, \text{Sm}, \text{Gd}$ ) for the electrode in solid oxide fuel cells *Solid State Ionics* (1999) C.-Y. Gu et al.
- [46] High performance Ca-containing  $\text{La}_{2-x}\text{Ca}_x\text{NiO}_{4+\delta}$  ( $0 \leq x \leq 0.75$ ) cathode for proton-conducting solid oxide fuel cells *Int. J. Hydrog. Energy* (2020) N.A. Baharuddin et al.
- [47] Short review on cobalt-free cathodes for solid oxide fuel cells *Int. J. Hydrog. Energy* (2017)
- [48] J. Tong et al.
- [49] Investigation of ideal zirconium-doped perovskite-type ceramic membrane materials for oxygen separation *J. Membr. Sci.* (2002) Z.P. Shao et al.
- [50] Advanced synthesis of materials for intermediate-temperature solid oxide fuel cells *Prog. Mater. Sci.* (2012) K.S. Baek et al.
- [51] Electrical conductivity characteristics of Sr substituted layered perovskite cathode ( $\text{SmBa}_{0.5}\text{Sr}_{0.5}\text{Co}_2\text{O}_{5+\delta}$ ) for intermediate temperature-operating solid oxide fuel cell *Ceram. Int.* (2022) A.I. Klyndyuk et al.
- [52] Structural and electrochemical characterization of  $\text{YBa}(\text{Fe}, \text{Co}, \text{Cu})_2\text{O}_{5+\delta}$  layered perovskites as cathode materials for solid oxide fuel cells *Int. J. Hydrog. Energy* (2021) S.L. Zhang et al.
- [53] Effect of Fe doping on the performance of suspension plasma-sprayed  $\text{PrBa}_{0.5}\text{Sr}_{0.5}\text{Co}_{2-x}\text{Fe}_x\text{O}_{5+\delta}$  cathodes for intermediate-temperature solid oxide fuel cells *Ceram. Int.* (2017) S. Yoo et al.
- [39] Investigation of layered Perovskite type  $\text{NdBa}_{1-x}\text{Sr}_x\text{Co}_2\text{O}_{5+\delta}$  ( $x=0, 0.25, 0.5, 0.75, \text{ and } 1.0$ ) cathodes for intermediate-temperature solid oxide fuel cells *Electrochim. Acta* (2013) A. Junet et al.
- [54] Optimization of Sr content in layered  $\text{SmBa}_{1-x}\text{Sr}_x\text{Co}_2\text{O}_{5+\delta}$  Perovskite cathodes for intermediate-temperature solid oxide fuel cells *Int. J. Hydrog. Energy* (2012) S. Choi et al.
- [55] Electrochemical properties of an ordered Perovskite  $\text{LaBaCo}_2\text{O}_{5+\delta}\text{-Ce}_{0.9}\text{Gd}_{0.1}\text{O}_{2-\delta}$  composite cathode with strontium doping for intermediate-temperature solid oxide fuel cells *Electrochim. Commun.* (2013) H.P. Ding et al.
- [56]  $\text{PrBa}_{0.5}\text{Sr}_{0.5}\text{Co}_2\text{O}_{5+\delta}$  layered perovskite cathode for intermediate-temperature solid oxide fuel cells *Electrochim. Acta* (2010) F. Zhao et al.
- [57] Layered perovskite  $\text{PrBa}_{0.5}\text{Sr}_{0.5}\text{Co}_2\text{O}_{5+\delta}$  as high performance cathode for solid oxide fuel cells using oxide proton-conducting electrolyte *J. Power Sources* (2010) F.J. Jin et al.
- [58] Characterization and evaluation of double Perovskite  $\text{LnBaCoFeO}_{5+\delta}$  ( $\text{Ln}=\text{Pr and Nd}$ ) as intermediate-temperature solid oxide fuel cell cathodes *J. Power Sources* (2013)



10.22214/IJRASET



45.98



IMPACT FACTOR:  
7.129



IMPACT FACTOR:  
7.429



# INTERNATIONAL JOURNAL FOR RESEARCH

IN APPLIED SCIENCE & ENGINEERING TECHNOLOGY

Call : 08813907089  (24\*7 Support on Whatsapp)